Polymer 298 (2024) 126885

Contents lists available at ScienceDirect

Polymer

journal homepage: www.elsevier.com/locate/polymer

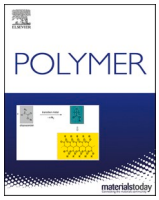

Drug delivery with melt-spun liquid-core fibers

Moritz Röthlisberger [a], Sithiprumnea Dul [a], Philipp Meier [b], Giorgia Giovannini [c], Rudolf Hufenus [a], Edith Perret [a,d,*]

[a] Laboratory for Advanced Fibers, Empa, Swiss Federal Laboratories for Materials Science and Technology, Lerchenfeldstrasse 5, 9014 St. Gallen, Switzerland
[b] Laboratory for Particles-Biology Interactions, Empa, Swiss Federal Laboratories for Materials Science and Technology, Lerchenfeldstrasse 5, 9014 St. Gallen, Switzerland
[c] Laboratory for Biomimetic Membranes and Textiles, Empa, Swiss Federal Laboratories for Materials Science and Technology, Lerchenfeldstrasse 5, 9014 St. Gallen, Switzerland
[d] Center for X-ray Analytics, Empa, Swiss Federal Laboratories for Materials Science and Technology, Überlandstrasse 129, 8600, Dübendorf, Switzerland

ARTICLE INFO

Keywords:
Liquid-filled fibers
Drug delivery
Medical applications
Melt-spinning

ABSTRACT

Conventional local drug delivery systems often encounter issues such as burst-release, limited drug reservoirs, rigidity, and low mechanical performance. We present an innovative approach to local drug delivery utilizing melt-spun drug-loaded liquid-core filaments (LiCoFs). LiCoFs were produced, incorporating fluorescein sodium salt as the model drug, dissolved in various liquid core materials, and enveloped by poly(ε-caprolactone) as the sheath material. We assessed thermal, mechanical, and structural properties of LiCoFs and have conducted extensive drug diffusion trials. Some trials involved pre-exchange of the liquid core with ibuprofen, bovine serum albumin–fluorescein isothiocyanate and methylene blue solutions using a pumping device. It was observed that diffusion mechanisms and diffusion rates depend on temperature, core size/sheath thickness, sheath permeability, carrier liquid type, drug molecule properties, and the drug's affinity to the sheath polymer. These drug-loaded LiCoFs pave the way towards a new generation of medical textiles facilitating controlled, local drug delivery.

1. Introduction

Many conventional drug delivery routes, including injection, parenteral, oral, sublingual, inhalation, suppository, implant, or topical pathways exist. Local drug delivery systems offer several advantages over conventional delivery routes; (i) controlled, constant, and targeted drug release, (ii) enhanced efficacy by delivering higher doses to specific sites, (iii) reduced systemic side effects and minimized impact on adjacent healthy tissues and organs and, (iv) depending on the biodegradability, no additional surgery for device removal is needed [1]. The field of "textiles for drug delivery" is rapidly growing in personalized medicine, with the potential to revolutionize local drug delivery methods, offering greater efficiency and convenience in drug administration. In conventional drug delivery textiles, fibers or textiles are loaded with bioactive agents or drugs using physical or chemical processes, such as absorption, coating, encapsulation, grafting or covalent conjugation [2], particularly for transdermal applications [2–9]. Current research primarily focuses on developing smart stimuli-responsive textiles capable of releasing drugs on demand, triggered by external factors such as ultrasound, pH, temperature or electrical fields [2,10].

We introduce an innovative drug delivery method, based on drug-loaded melt-spun liquid-core filaments (LiCoFs). Empa has developed a technique for melt-spinning polymer fibers that can continuously encase, during production, a liquid core containing a drug [11,12]. Recently, this method has been successfully scaled up, and the industry has produced the first LiCoFs [13,14]. LiCoFs, with diameters ranging from 50 to 200 μm, hold immense potential for diverse applications, including pressure sensors [14], robotics, optical fibers [15] and local drug delivery. Melt-spun fibers have significantly larger diameters, higher mechanical performance and durability compared to fibers produced by electrospinning [16] or force-spinning (centrifuge spinning or pressurized gyration) [17]. These properties allow melt-spun filaments to be processed into textiles, such as woven and knitted fabrics. In contrast to durable woven or knitted fabrics, nanofiber mats are primarily appealing for specific applications such as tissue engineering due to their extensive surface area and high porosity [18–20]. In a few cases,

* Corresponding author. Laboratory for Advanced Fibers, Empa Swiss, Federal Laboratories for Materials Science and Technology, Lerchenfeldstrasse 5, 9014 St. Gallen, Switzerland.
E-mail address: edith.perret@empa.ch (E. Perret).

https://doi.org/10.1016/j.polymer.2024.126885
Received 22 October 2023; Received in revised form 26 February 2024; Accepted 5 March 2024
Available online 6 March 2024

co-axial electrospinning or force-spinning has been utilized to integrate drugs into nanofibers [16,17]. However, to the best of our knowledge, this article reports for the first time a direct drug incorporation using a liquid-core melt-spinning technique. It's essential to note that, unlike electrospinning or force-spinning, melt-spinning is the most cost-effective and industrially applied method for mass-producing monofilaments exceeding 20 μm in size [21,22].

The liquid-core melt-spinning technique can be used to produce biocompatible drug-loaded LiCoFs in a continuous way. Depending on factors such as the size (molecular weight) and hydrophobicity of drug molecules, drugs can follow different release mechanisms. They may either diffuse through the polymer sheath in a controlled, diffusion-driven manner (for small molecules) or be transported along the fiber core to the fiber's end (for larger molecules). Fig. 1 illustrates potential applications for such fibers. These fibers could be implanted into the body with a connection to an external reservoir, enabling precise local drug delivery to specific body locations. Moreover, these fibers could serve various purposes, such as; (i) acting as surgical suture materials for both internal and external injuries [23], (ii) serving as grafts [24], (iii) functioning as supplementary fibers for other medical devices, e.g., nerve guidance conduits [25,26], or (iv) being utilized for implantable or transdermal textiles [6] designed for local drug delivery applications [27,28]. These textiles could provide benefits such as, anti-inflammatory, anti-microbial [29], anti-coagulant and potentially anti-ageing effects.

To melt-spin drugs directly into the core of a filament, they must withstand the high processing temperature of the polymer. Alternatively, a drug-free liquid core can be exchanged with a drug-containing liquid. This approach allows for spinning trials or offline liquid exchanges with various drugs. Some examples include ibuprofen, corticosteroids, antibiotics, insulin, anti-coagulants, vitamins, enzymes, natural oils, cooling agents (menthol), hyaluronic acid, retinol or nanocarriers such as nanoparticles, liposomes, dendrimers or cyclodextrins [30]. Compared to conventional drug delivery methods, LiCoFs offer several advantages. They are flexible, can be woven into textiles and possess a substantial drug reservoir. The ultimate goal is to develop textiles capable of delivering drugs on demand with strategic placement, depending on the patient's needs.

In this article, we present the proof-of-concept for melt-spinning of drug-loaded LiCoFs, and conduct drug diffusion trials. Fluorescein sodium salt was selected as the model drug and was dissolved in various liquids. Different carrier liquids were utilized to assess their spinnability (compatibility with the sheath material) and to investigate how the core carrier liquid affects the diffusion behavior of fluorescein sodium salt. Poly(ε-caprolactone) (PCL) was chosen as the polymeric sheath material. Several filaments with different liquid core materials and numerous inner/outer diameters have been produced. Several analytical tests have been performed to comprehensively understand the material and fiber properties. The rheological properties of liquids and the polymer have been investigated. Mechanical, thermal and structural properties have been studied with tensile tests, differential scanning calorimetry (DSC), scanning electron microscopy (SEM) and x-ray analytics. Diffusion trials, involving fluorescence spectroscopy, have been performed in order to determine the release of fluorescein from the filaments. Further studies were accomplished to evaluate the exchange of liquid cores with other solutions containing drugs (ibuprofen), labeled proteins (bovine serum albumin–fluorescein isothiocyanate, BSA-FITC), as well as a chromophores (methylene blue containing liquid, Aqua stabil). The diffusion of the loaded compounds was analyzed using either Ultra Performance Liquid Chromatography (UPLC), fluorescence spectroscopy or ultraviolet–visible (UV–vis) spectroscopy.

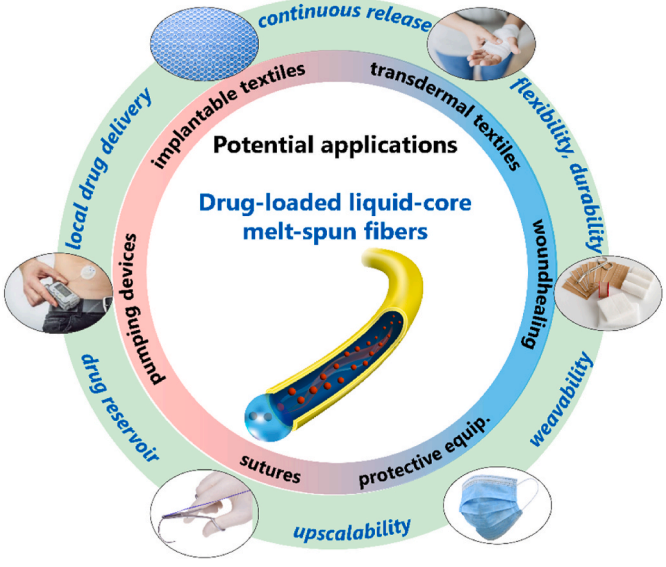

Fig. 1. Potential applications of drug-loaded melt-spun liquid-core fibers. Images: "Todor Rusinov, Chutidech, Womue, Rawpixel.com, Andrew Norris - stock.adobe.com, Roman Zaiets/Shutterstock.com".

2. Materials and methods

2.1. Materials for melt-spinning

A thermoplastic high-molecular weight (Mw = 50′000 Da) poly (ε-caprolactone) (PCL) in the form of pellets, Capa™ 6500 (Perstorp Holding AB, Malmö, Sweden), was used in the co-extrusion for the sheath material of the LiCoFs. The data sheet indicates a melting temperature of 60 °C and a melt flow index of 7 g/10 min at 160 °C with 2.16 kg. It has a density of 1.1 g/cm3 at 25 °C. Several liquid core carrier materials have been co-extruded and are summarized in Table 1. The selection of liquids was based on their biocompatibility with the human body. To serve as a fluorescent tracer in the liquid core, we incorporated fluorescein sodium salt (F6377, Sigma-Aldrich, St. Louis, USA), referred to as 'f' throughout the rest of this manuscript. Typically a concentration of 0.01 wt% of fluorescein sodium salt was used. Additionally, some LiCoFs were melt-spun either without a tracer or with a higher concentration of fluorescein sodium salt at 0.1 wt%.

2.2. Melt-spinning of LiCoFs

The melt-spinning of both PCL monofilaments and LiCoFs was conducted using a custom-made pilot plant. This setup comprised a 16 mm, 30 L/D single screw-extruder (Collin Lab & Pilot Solutions GmbH, Maitenbeth, Germany), a spin pack (designed in-house [14]), a water bath (designed in-house), a quenching chamber (Fourné Maschinenbau GmbH, Alfter, Germany) and a filament draw-down unit (designed in-house), as illustrated in Fig. 2. For the production of LiCoFs, a high pressure syringe pump (Telegyne ISCO 260D from SCF processing LTD, Drogheda, Ireland) was utilized to inject the liquid core [12] (Fig. 2). To facilitate rapid quenching of the polymer melt and enhance the draw strength of LiCoFs, a water bath of approximately 15 °C was positioned 4–6 cm below the spinneret die.

The PCL pellets were introduced into the feed hopper and then extruded through various heating zones within the extruder. This process involved a feeding zone set at 30 °C, followed by zones with temperatures set to 100 °C. For PCL monofilament spinning, the die capillary had a length of 4 mm and a diameter of 1.0 mm (L/D = 4). In the case of LiCoFs, the spinneret die capillary also measured 4 mm in length with a diameter of 1.0 mm (L/D = 4), and the internal capillary for the liquid injection had an outer diameter of 0.7 mm and an inner diameter of 0.5 mm (inset Fig. 2). Further information regarding the LiCoF spin pack is available elsewhere [14].

Multiple fibers have been produced by employing different liquid

Table 1
Liquid core carrier materials of LiCoFs.

Label	Name	Supplier	Product name or number	M_w (g/mol)	Density @ 20–25 °C (g/cm^3)
Glycerol	Glycerol (99+%, extra pure)	Thermo Fischer Scientific	158922500	92	1.26
PEG 200	Poly(ethylene glycol)	Sigma-Aldrich	8.17001	200	1.124
solPEG 200′000	5 wt% of Poly(ethylene glycol) mixed with water	DuPont	POLYOX™ WSR N80	200′000	Not measured
mPEG 500	Poly(ethylene glycol) methyl ether	Sigma-Aldrich	81316	500	1.07
mPEG 750	Poly(ethylene glycol) methyl ether	Sigma-Aldrich	81319	750	1.094

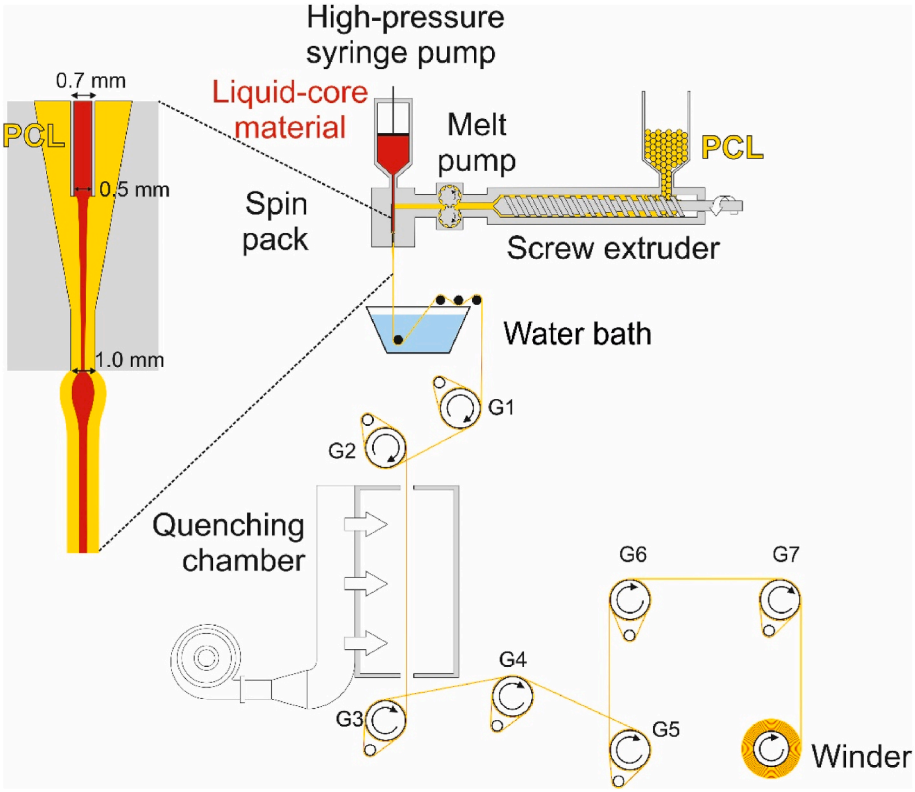

Fig. 2. Melt-spinning setup for the production of liquid core fibers. G1 through G7 indicate the seven godets of the draw-down unit.

Table 2
Produced monofilaments and LiCoFs with corresponding melt-spinning parameters.

Label	Empa fiber no.	Liquid core	Liquid throughput (ml/min)	High-pressure syringe pump (bar)	Spin pressure (bar)	Polymer mass throughput (g/min)
PCL_monofil	2346	NA	NA	NA	127	6.6
PEG200_vlc	2356	PEG Mw 200	1.2	95	147	7.9
PEG200_sc	2357	PEG Mw 200	1.2	95	147	7.9
PEG200f_vlc	2358	PEG Mw 200, 0.01 wt% f	1.2	95	146	7.9
PEG200f_sc	2360	PEG Mw 200, 0.01 wt% f	1.2	102	166	10.6
PEG200f_lc	2361	PEG Mw 200, 0.01 wt% f	1.8	102	166	
mPEG500f_sc	2362	mPEG Mw 500, 0.01 wt% f	1.2	102	167	
mPEG500f_lc	2363	mPEG Mw 500, 0.01 wt% f	1.8	103	167	
mPEG500_hf_sc	2364	mPEG Mw 500, 0.1 wt% f	1.2	102	169	
mPEG500_hf_lc	2365	mPEG Mw 500, 0.1 wt% f	1.8	102	168	
mPEG750f_sc	2370	PEG Mw 750, 0.01 wt% f (heated to 40 °C)	1.2	107	166	
mPEG750f_lc	2371	PEG Mw 750, 0.01 wt% f (heated to 40 °C)	1.8	107	164	
sol5%PEG_f_sc	2366	5 wt% PEG Mw 200′000 in water, 0.01 wt% f	1.2	102	170	
sol5%PEG_f_lc	2367	5 wt% PEG Mw 200′000 in water, 0.01 wt% f	1.8	102	169	
glycerol_f_sc	2368	Glycerol, 0.01 wt% f	1.2	105	168	
glycerol_f_lc	2369	Glycerol, 0.01 wt% f	1.8	106	168	

cores and adjusting melt-spinning parameters. Details regarding the spinning parameters, including the liquid core material, throughputs, and pressures for a chosen set of produced filaments are reported in Table 2. The labels 'vlc, lc, sc' stand for 'very large core', 'large core' and 'small core', respectively.

Details of the drawing parameters, which encompass godet speeds and temperatures, along with the calculated draw ratio (the ratio of the speed of the final godet 7 to the take-up godet 1), are provided in Table 3. Both the take-up speed (the speed of godet 1) and the draw ratio (DR) affect the fineness of the produced filament. Molecular orientation begins during the draw-down phase between the spinneret die and the first godet, but the majority of molecular orientation is induced during the drawing process between godet 2 and godet 3 to achieve highly drawn filaments (DR $\geq$ 5.0).

2.3. Materials for diffusion trials

Phosphate-buffered saline (PBS) (10 mM) solution was prepared by solubilizing NaCl (0.137 M), KCl (2.7 mM), Na_2PO_4 (0.01 M) and KH_2PO_4 (1.8 mM) in distilled water. The pH was adjusted to 7.4 by adding NaOH or HCl. All raw materials were purchased from Sigma-Aldrich (Merck, Switzerland).

2.4. Liquid exchange

To investigate the diffusion of molecules, other than fluorescein sodium salt, from the fibers, we carried out a core liquid exchange with various drug solutions. This exchange process involved placing fiber bundles into a plastic tube, which was sealed by bonding with epoxy adhesive (Rapid Araldite). After allowing at least 12 h for the bonding to set, the tip of the tube was carefully cut using a sharp razor blade to expose the liquid cores. Subsequently, the tube was connected to a hydraulic pump (Matter Hydraulik AG, Ellikon an der Thur, Switzerland), operating at pressures of up to 2 bar.

The following drug solutions were used for the liquid exchange:

i) A solution of 0.1 wt% ibuprofen (I4883, Sigma-Aldrich, Merck, Switzerland) dissolved in mPEG 500.
ii) Aqua stabil (Julabo, Seelbach, Germany), a water bath protective medium containing methylene blue (~0.004 wt%).
iii) A 1 wt% bovine serum albumin–fluorescein isothiocyanate (BSA-FITC) conjugate (A9771, Sigma-Aldrich, Merck, Switzerland) dissolved in a physiological sodium chloride solution (07982, Sigma-Aldrich, Merck, Switzerland).

Note that we initially conducted a diffusion trial with 0.01 wt% of ibuprofen dissolved in mPEG 500. However, the concentration of diffused ibuprofen proved to be too low for reliable detection using UPLC. Consequently, we opted for a higher concentration (0.1 wt%) for this specific liquid exchange.

2.5. Diffusion trials

2.5.1. Diffusion trials of fluorescein sodium salt with fluorescence spectroscopy

Two types of diffusion trials were conducted, as illustrated in Fig. 3. One trial involved cut fiber pieces immersed in PBS (Fig. 3a), to evaluate the migration of fluorescein along the liquid core. In this experiment, bundles of each filament type (20x) were cut into 1 cm long pieces and placed into Eppendorf safe-lock tubes. For each filament type, four safe-lock tubes were prepared, each containing twenty 1 cm pieces. A phosphate-buffered saline (PBS) solution was then prepared, and 0.5 ml was added to each tube. Two of the safe-lock tubes for each filament type were left at room temperature for 24 h, while the other two were immersed for 24 h in a heated water bath at 37 °C to simulate body temperature. The second trial aimed to determine whether fluorescein diffuses through the polymer sheath. For this purpose, we prepared seven loops for each filament type, attaching the filament bundles on the exterior of the lock tube (Fig. 3b). Seven loops were selected because the estimated length of an immersed filament loop in 0.5 ml was approximately 3 cm, resulting in a total length of about 21 cm. Note that the effective length always varied a little bit. Additionally, the fiber parts above the liquid contained a drug reservoir. Like the first trial, four tubes were prepared per filament type for the diffusion experiments, with two tubes for trials at room temperature and two for trials at an elevated

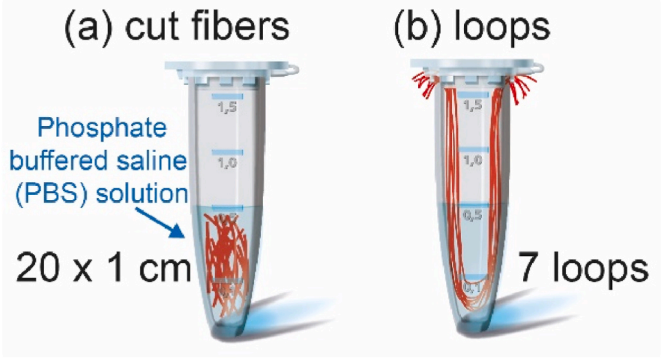

Fig. 3. Diffusion trial types: safe-lock tubes with (a) cut fiber pieces and with (b) filament loops. (Adapted image from "Irbis-Nariel – stock.adobe.com").

Table 3
Drawing parameters.

Label	Godet 1	Godet 2	Godet 3	Godet 4	Godet 5	Godet 6	Godet 7	Winder	Draw ratio, DR
	speed/temperature (m/min, °C)								
PCL_monofil	40/25	41/25	220/30	260/25	260/25	260/25	260/25	260	6.5
PEG200_vlc	100/30	101/30	105/45	107/30	107/30	110/20	110/20	105	1.1
PEG200_sc	100/30	101/30	360/45	360/30	355/30	360/20	360/20	360	3.6
PEG200f_vlc	110/30	110/30	115/45	118/30	118/30	120/20	120/20	120	1.1
PEG200f_sc	80/25	85/25	370/45	380/40	390/30	400/30	400/25	390	5.0
PEG200f_lc									
mPEG500f_sc									
mPEG500f_lc									
mPEG500_hf_sc									
mPEG500_hf_lc									
mPEG750f_sc									
mPEG750f_lc									
sol5%PEG_f_sc									
sol5%PEG_f_lc									
glycerol_f_sc									
glycerol_f_lc									

temperature of 37 °C.

The extent of fluorescein release was subsequently determined by quantifying the amount of fluorescein in the PBS solution using a fluorescent spectrophotometer (Cary Eclipse, Agilent, Santa Clara, CA, USA) with an excitation wavelength of 490 nm. In each experiment, 100 μL of the PBS solutions (following 24 h of diffusion) was added in a 96-well plate. The resulting spectra were recorded, and a spectrum of the blank (pure PBS) was subtracted from the measured spectra. The maximum peak intensities observed near 515 nm were converted into concentrations (μmol/l) by employing a linear calibration curve, which was established by measuring various concentrations of fluorescein in PBS (see supporting information). Note that the appropriate excitation wavelength (490 nm) was determined in advance using a UV–vis spectrophotometer (Varian 50Bio connected to 50 MPR, Agilent, Santa Clara, CA, USA) measuring fluorescein containing PBS solutions.

2.5.2. Diffusion trials of ibuprofen with UPLC UV–vis

For LiCoFs in which the core liquid was exchanged with ibuprofen solutions, the fibers were cut into thirty pieces, each measuring 1 cm in length, and then placed into Eppendorf tubes. Subsequently, these tubes were filled with 0.75 ml of PBS. We opted for 0.75 ml for these diffusion trials because initially a larger volume of liquid was required for UPLC testing. As for the loops, 0.5 ml of PBS was added to the seven loops. Once again, four safe-lock tubes were prepared for each cut fiber sample, along with four for the loops (two for room temperature trials and two for trials at 37 °C).

Since ibuprofen is not fluorescent, we employed UPLC coupled with UV–vis spectroscopy to determine the quantity of diffused ibuprofen. The UPLC system utilized was an Acquity UPLC (Waters Inc., Baden, Switzerland), equipped with a UV–vis spectrometer. Separation was achieved through reverse-phase gradient elution transitioning from 95/5% to 5/95% (v/v) water/acetonitrile with the addition of 0.1% formic acid over a 5-min interval. The mobile phase was delivered at a flow rate of 0.5 ml min^{-1} through an Acquity C18 column (2.1 mm × 50 mm, 1.7 μm) maintained at 40 °C. An injection volume of 10 μl was used and a UV–vis spectrum in the range of 210–475 nm was acquired and integrated for each retardation time. Calibration curves can be found in the supporting information.

2.5.3. Diffusion trials of methylene blue with UV–vis spectroscopy

The liquid cores of melt-spun LiCoFs containing PEG 200 (PEG200f_vlc, PEG200f_sc, PEG200f_lc) were exchanged with Aqua stabil. The subsequent sample preparation for diffusion trials followed the same procedure as that for the melt-spun LiCoFs containing fluorescein in their cores. In each case, 100 μL of the solution was filled into a 96-well plate, and the amount of diffused methylene blue was determined using a UV–vis spectrophotometer (Varian 50Bio connected to 50 MPR, Agilent, Santa Clara, CA, USA). This determination was made by comparing the values of the absorption peak height, at approximately 663 nm, above a linear background with the calibration curve for Aqua stabil in PBS (refer to the supporting information).

Additionally, another experimental setup was employed to assess the diffusion of methylene blue from a reservoir of high concentration of methylene blue to pure water through a connection made with the LiCoF PEG200_vlc (these results are only shown in the supporting information). Prior to establishing the connection, the fiber was pre-flushed with water.

2.5.4. Diffusion trials of BSA-FITC with fluorescence spectroscopy

The cores of LiCoFs, specifically PEG 200 containing ones (PEG200_vlc, PEG200_sc) without fluorescein were subjected to a liquid exchange with BSA-FITC salt solutions. It was necessary to use fibers devoid of fluorescein to ensure that no other fluorescent tracer was present in the fibers. The subsequent sample preparation for diffusion trials followed the identical procedure used for the diffusion trials of LiCoFs containing fluorescein in the cores. The extent of BSA-FITC release was determined by measuring the amount of BSA-FITC present in the PBS solution three times using a fluorescent spectrophotometer (Cary Eclipse, Agilent, Santa Clara, CA, USA) with an excitation wavelength of 495 nm. The same measuring procedure was followed as for fluorescein. Calibration curves are available in the supporting information.

2.6. Characterization

2.6.1. Rheology

Rheology measurements were conducted using a Physica MCR 301 rheometer (Anton Paar, Graz, Austria), with a plate-plate geometry (diameter 25 mm) for PCL samples and a cone-plate geometry (diameter 50 mm) for the liquid materials. Gap distances between the plates were set to 1 mm and 0.1 mm, respectively. For PCL, rheological properties were determined with amplitude, frequency and time sweeps at constant temperatures of 90 °C, 100 °C, 110 °C and 120 °C. During amplitude sweeps, the angular frequency was kept constant ($\omega = 1$ rad/s), while the applied strain percentage was increased from 0.1% to 500%. These amplitude sweeps allowed for the identification of the linear viscoelastic region. Frequency sweeps provided information about the sample's response (complex viscosity, storage and loss moduli) to angular frequency, ranging from 0.01 rad/s to 500 rad/s, at a constant strain of 5%. Time sweeps, with strain and angular frequency held constant ($\gamma = 1\%$, $\omega = 1$ rad/s, $t = 30$ min), were performed to assess the thermal stability of the polymer.

Regarding the liquid core materials, temperature sweeps were carried out at a shear rate of $\dot{\gamma} = 100\ s^{-1}$ and with a heating rate of 10 °C/min. Additionally, time sweeps were conducted at 25 °C, 37 °C, and at either 80 °C or 100 °C to verify the viscosity values obtained from temperature sweeps.

2.6.2. Scanning electron microscopy

A bundle of fibers was threaded through a metal plate hole with a diameter of 1.0 mm and was then cut using a sharp razor blade. The cross-sectional profiles of the fibers were subsequently examined using a scanning electron microscope (SEM) (Hitachi S-4800, Hitachi High-Technologies, Krefeld, Germany). Typical acceleration voltages of 2 kV were employed for the SEM analysis. To mitigate extensive charging effects, the samples were sputter-coated with a 10 nm thick layer of Au/Pd (EM ACE 600, Leica, Switzerland).

2.6.3. Mechanical testing

A subset of melt-spun LiCoFs have been characterized using a Zwick Z100 (Zwick Roell GmbH, Germany) tensile testing machine. Pneumatic clamps were used to secure the LiCoFs firmly, preventing any slipping [22]. An initial distance of 100 mm was established between the clamps, and a 10 N load cell was used. The elongation rate was set to 100 mm/min, in accordance with the ASTM D 2256 standard procedures.

2.6.4. Differential scanning calorimetry

The thermal properties of the raw materials (PCL pellets and liquids), as well as those of melt-spun PCL monofilaments and LiCoFs, were characterized using differential scanning calorimetry (DSC) with the DSC 214 Polyma instrument (NETZSCH-Gerätebau GmbH, Selb, Germany). These measurements were conducted in a nitrogen atmosphere. Each sample underwent a heating-cooling-heating cycle spanning from 40 °C to 160 °C, with ramping rates of ±10 °C/min. The crystallinity of the PCL sheath in the LiCoFs was determined based on the melt enthalpy of the first heating cycle, as per Equation (1).

$$\chi(\%) = \frac{\Delta H^{PCL}_{m,meas} \bullet m^{fiber} \Big/ m^{sheath}}{\Delta H^{PCL}_{m,ref}} \times 100 = \frac{\Delta H^{PCL}_{m}}{\Delta H^{PCL}_{m,ref}} \times 100 \qquad \text{(Eq. 1)}$$

The measured melting enthalpy, $\Delta H^{PCL}_{m,meas}$, needed to be corrected for the effective weight of the considered sheath material. The ratio

Table 4
Filament and core diameters as well as measured fineness values.

Label	Filament diameter (μm)	Core diameter (μm)	Measured fineness (tex = mg/m)[a]	Comments
PCL_monofil	171 ± 4	NA	25.0	reference
PEG200_sc	172 ± 6	56 ± 3	23.8	leakage
PEG200_vlc	304 ± 5	116 ± 5	80.2	leakage
PEG200f_vlc	288 ± 4	107 ± 1	71.7	leakage
PEG200f_sc	180 ± 1	62 ± 5	27.9	leakage
PEG200f_lc	187 ± 1	75 ± 3	29.5	leakage
mPEG500f_sc	181 ± 1	60 ± 4	28.0	no leakage
mPEG500f_lc	188 ± 1	74 ± 1	29.7	no leakage
mPEG500_hf_sc	181 ± 1	60 ± 5	28.1	no leakage
mPEG500_hf_lc	187 ± 2	75 ± 7	29.3	no leakage
mPEG750f_sc	181 ± 1	62 ± 4	27.7	leakage
mPEG750f_lc	188 ± 2	76 ± 5	29.5	leakage
sol5%PEG_f_sc	182 ± 2	62 ± 4	24.0	no leakage
sol5%PEG_f_lc	187 ± 1	73 ± 4	24.3	no leakage
glycerol_f_sc	181 ± 1	61 ± 4	28.0	leakage
glycerol_f_lc	188 ± 2	74 ± 3	29.5	leakage

[a] Measuring inaccuracy is below ± 0.6 tex.

between the fiber mass and the mass of the sheath was estimated based on measured fiber and core diameters (Table 4) and density values provided in Table 1. The enthalpy, $\Delta H^{PCL}_{m,ref} = 139.5$ J/g, corresponding to 100% crystalline PCL was obtained from literature sources [31].

2.6.5. X-ray measurements

Wide-angle x-ray diffraction (WAXD) and small-angle x-ray scattering (SAXS) patterns of both PCL monofilaments and LiCoFs were acquired using a Bruker Nanostar U diffractometer (Bruker AXS, Karlsruhe, Germany). The instrument featured a beam defining pinhole with a diameter of 300 μm, a Cu Kα radiation (λ = 1.5419 Å) and was equipped with a VÅNTEC-2000 MikroGap area detector. Single filaments were used for all WAXD and SAXS measurements, which were carried out in two separate experiments with sample-to-detector distances of 9.0 cm and 110.5 cm, respectively. WAXD patterns were collected for 30 min, while SAXS patterns were recorded for 1 h. The acquired WAXD/SAXS patterns were analyzed using the evaluation software DIFFRAC.EVA (version 4.2., Bruker AXS, Karlsruhe, Germany) in conjunction with Python codes. Peaks in azimuthal WAXD scans within the ring sector defined by ($21° < 2\Theta < 22°$) were fitted with Pearson VII distribution functions [32], employing Python codes. Hermans's equation [33] was applied to extract the orientation parameter $f_{(110)}$ of the crystals [34]. If $f_{(110)} = 1$, it indicates that the (110) planes of the crystals are perfectly aligned parallel to the fiber axis, whereas $f_{(110)} = 0$ signifies random crystal orientation. Long-spacings, coherence lengths and lamellar sizes were calculated by analyzing meridional and transversal areas of the SAXS pattern, following the approach utilized in prior publications on PCL fibers [34,35].

3. Results and discussion

3.1. Rheological properties of PCL

The dynamical rheological behavior of the PCL material (in pellet form) was assessed through isothermal frequency sweeps with a fixed strain $\gamma = 5\%$ conducted at temperatures of 90 °C, 100 °C, 110 °C and 120 °C. The results, summarized in Fig. 4, are consistent with previously published data on the same material in powder form [36]. A characteristic Newtonian plateau is observed in the complex viscosity (Fig. 4a), along with a shear-thinning region evident at higher frequencies. Notably, the loss modulus of PCL surpasses the storage modulus ($G'' > G'$), indicating a more fluid-like viscous behavior (Fig. 4b). The melt strength of PCL is directly correlated with the crossover point between G' and G''. A lower crossover point, both on the x and y axes, signifies higher melt strength. The melt strength of PCL is relatively poor, which makes it a challenging material for melt-spinning. In general, polymers characterized by a higher storage modulus compared to the loss modulus are preferred for extrusion processes, as this ensures that the material maintains its shape during extrusion. Furthermore, the Van Gurp-Palmen plot [37] (visible in the inset of Fig. 4b) reveals phase angles close to 90°, indicating a highly linear structure and a low polydispersity of the material.

We conducted amplitude and time sweeps at the same temperatures as those used for the frequency sweeps. The amplitude sweeps revealed that both the loss and storage moduli remained relatively constant within the strain range of 0.1%–200%. Beyond a strain of approximately 200%, there was a noticeable decline in the storage moduli, indicating a decrease in the material's elastic properties. In contrast, the time sweeps demonstrated that the complex viscosity, as well as the moduli, remained stable throughout the entire duration of the sweeping process, which extended for 30 min. Furthermore, we also measured the rheological properties, such as viscosities in relation to temperature, of the liquid core materials, and these results are provided in the supporting information.

3.2. LiCoF cross-sections

LiCoF overall and core diameters have been determined using scanning electron microscopy (SEM). An example of an SEM image, magnified to x80, for cut fibers containing glycerol in the small core (glycerol_f_sc) is provided in Fig. 5.

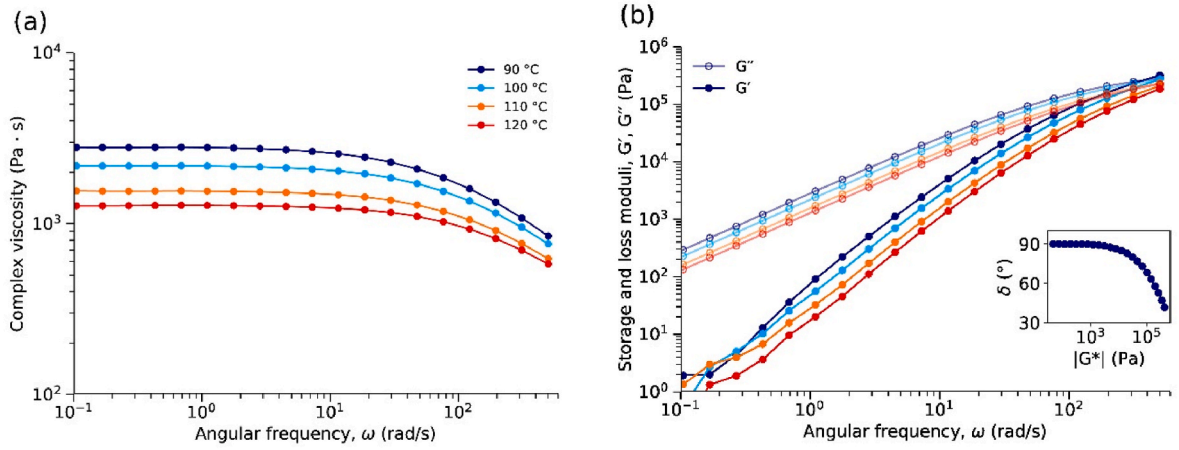

Fig. 4. Isothermal frequency sweeps: (a) complex viscosity, (b) storage (G' full symbols) and loss (G'' empty symbols) moduli. Inset: Van Gurp-Palmen plot for 90 °C.

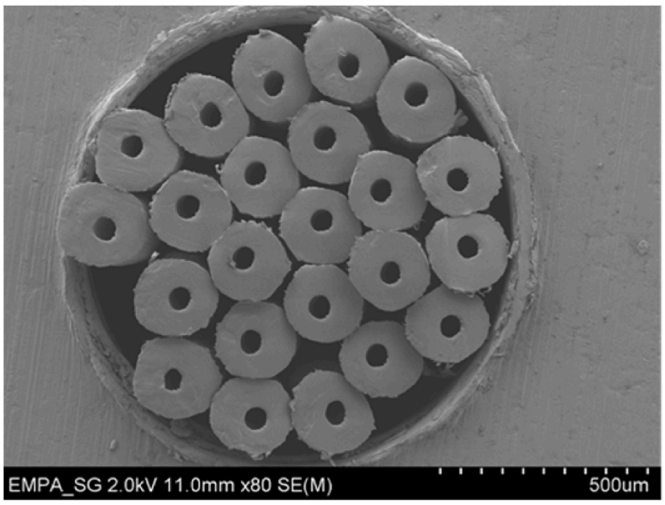

Fig. 5. SEM image of LiCoF glycerol_f_sc.

Ellipses were drawn over the SEM images using the imageJ software [38] to determine LiCoF overall and core diameters (supporting information). All determined filament and core diameters, along with measured fineness values, are presented in Table 4. Calculated fineness values from filament and core diameters, as well as from the density values given in Table 1, closely align with the measured fineness values. Table 4 also includes information about which LiCoFs exhibited some evidence of liquid leakage through the sheath. For those LiCoFs, wet traces from the core liquid were observed on the bobbins. This leakage likely occurred due to either the diffusion of small molecules, such as glycerol, or possibly due to small cracks in the sheath material.

3.3. Structure-mechanical property relationships

3.3.1. Mechanical properties

Mechanical properties were assessed for a chosen set of highly drawn filament types, with LiCoFs displaying significant liquid leakage being excluded from the measurement. The measured tensile force was divided by the calculated PCL sheath area to determine stress. Examples of measured stress-strain curves are illustrated in Fig. 6 for the PCL monofilament and for LiCoFs with mPEG 500 as the core. Among all the measured fiber samples, the PCL monofilament exhibits the highest tensile stress but the shortest elongation at break (Table 5). This is attributed to the fact that this filament underwent greater drawing during production, resulting in a higher degree of molecular orientation. The increased orientation in the PCL monofilament was confirmed by analyzing the azimuthal orientation in WAXD images of the (110)

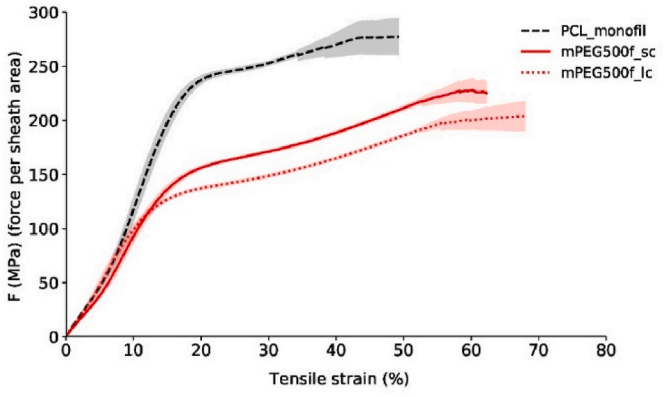

Fig. 6. Tensile properties of PCL monofilament and LiCoFs with mPEG 500 with small and large cores (sc/lc), respectively.

Table 5
PCL crystal orientation, ultimate tensile strength and elongation at break values.

Label	$f_{(110)}$ WAXD	PCL crystallinity (%)	UTS (ultimate force per sheath area) (MPa)	Elongation at break (%)
PCL_monofil	0.974	52 ± 1	278 ± 17	42 ± 4
mPEG500f_sc	0.973	53 ± 4	228 ± 9	58 ± 3
mPEG500f_lc	0.972	56 ± 1	204 ± 13	59 ± 4
mPEG750f_sc	0.971	52 ± 5	207 ± 7	69 ± 3
mPEG750f_lc	0.967	53 ± 1	195 ± 7	72 ± 3
sol5% PEG_f_sc	0.972	49 ± 1	208 ± 8	60 ± 2
sol5% PEG_f_lc	0.971	49 ± 0	208 ± 8	65 ± 3

reflection. It's essential to note that the LiCoFs couldn't be subjected to more extensive drawing in a single online step, as this led to breakage. The filament filled with mPEG 500, featuring a small core, achieved the highest ultimate tensile strength among all the measured LiCoFs. WAXD analysis revealed that LiCoFs with small cores (Fig. 6, solid line) exhibited higher molecular orientations in the PCL sheath (Table 5), resulting in higher tensile strengths compared to LiCoFs with large cores (Fig. 6, dotted line).

Given the low spinning speeds employed, the PCL monofilament exhibits a reasonable ultimate tensile stress (UTS) of approximately 278 MPa and an elongation at break of 42%. In comparison, standard melt-spun filaments, like polyethylene terephthalate (PET) filaments, typically attain UTS values ranging from 290 to 470 MPa at spinning speeds of about 4000 m/min, with ultimate tensile strains of approximately 110–125% [21]. Compared to fully drawn poly-4-hydroxybutyrate (P4HB) fibers [39], which are on the market for surgical sutures (UTS: 580–800 MPa and ε_{break}: 25–90%), PCL monofilaments or LiCoFs have a lower tensile strength. The tensile strength is significantly influenced by processing history, including factors such as orientation and crystallization, as well as the specific material type. While these initial trials have involved PCL, future experiments may explore other biocompatible polymers.

3.3.2. Structural properties (WAXD/SAXS analysis)

WAXD patterns were obtained for both the PCL monofilament and all LiCoFs (supporting information). A selection of these patterns is presented in Fig. 7, along with the proposed crystal structure according to Chatani et al. [40]. The crystal unit cell has lattice parameters $a = 7.47$ Å, $b = 4.98$ Å and $c = 17.05$ Å, with the molecular chain axis aligning along the c-axis. The PCL monofilament features highly oriented crystals. The peaks in Fig. 7a can be attributed to specific lattice planes [40]. In the case of marginally drawn LiCoFs (PEG200f_vlc), there is a lower degree of crystal orientation in the PCL sheath, as evident from the arc-like reflections observed in Fig. 7b. For highly drawn LiCoFs (mPEG500f_lc, mPEG750f_lc), an amorphous halo resulting from the polymeric liquid core material overlaps with the reflections originating from the highly oriented PCL sheath material, as depicted in Fig. 7c and d. In the case of mPEG 750, the halo is more pronounced compared to mPEG 500 due to the higher density of the core material.

Orientation parameters were determined using Hermans's equation [33] for the (110) crystalline planes and are summarized in Table 5, along with calculated crystallinities derived from DSC measurements (supporting information), ultimate tensile strengths, and elongation at breaks. The DSC curves for PCL monofilaments, LiCoFs, and their respective raw materials (PCL and liquid core materials) are presented in the supporting information. Overall crystallinity values were in the range of 49–56% demonstrating a relatively uniform crystallinity across all LiCoFs.

The highest degree of molecular orientation was observed for the PCL monofilament, and LiCoFs with smaller cores exhibited higher molecular orientation compared to those with large cores. Additionally,

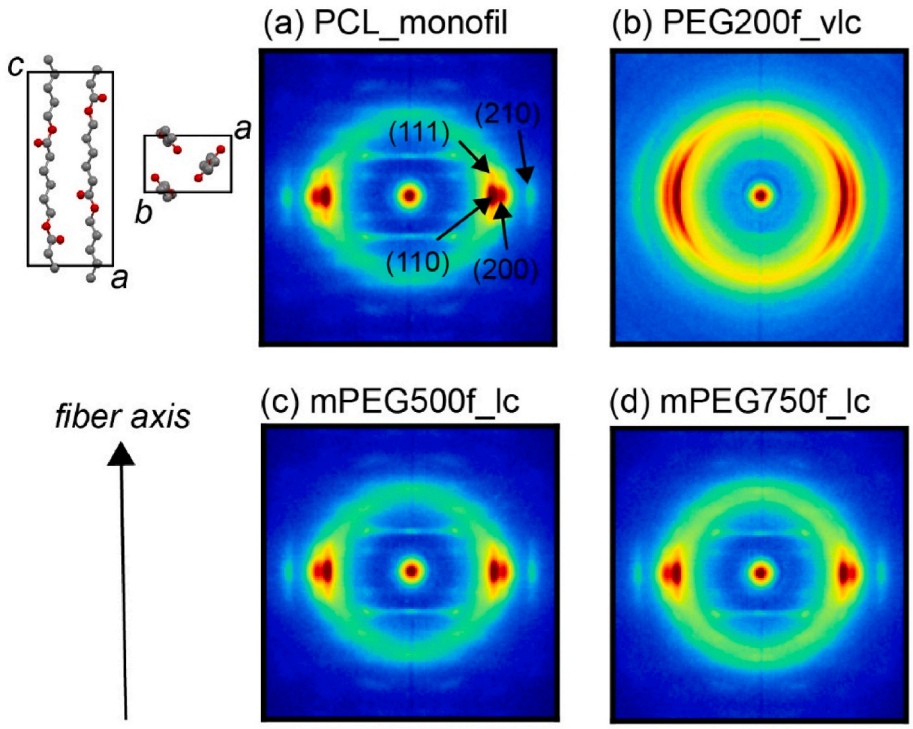

Fig. 7. PCL unit cell projected along *b*- and *c*-axis [40,41]. WAXD patterns of (a) PCL monofilament and LiCoFs: (b) less-oriented PEG200f_vlc, (c) mPEG500f_lc and (d) mPEG750f_lc.

filaments featuring mPEG750 or sol5%PEG cores displayed slightly lower orientation of PCL crystals, resulting in lower tensile strength. Orientation parameters for all LiCoFs can be found in the supporting information. To conclude, physical properties of the core liquid, such as thermal conductivity and viscosity, as well as the interaction between core and sheath materials, influence the crystal orientation of PCL and consequently impact the mechanical properties of the filaments. Similar findings have been reported in previous studies on bicomponent melt-spinning [42–44]. Additionally, the presence of a mesophase (non-crystalline but highly oriented molecular chains) may also affect the mechanical properties, as previously reported for PCL [34,35], poly (hydroxybutyrate-*co*-3-hexanoate) (PHBH) [45] and poly-3-hydroxybutyrate (P3HB) [46–53].

A selection of measured SAXS patterns is presented in Fig. 8, along with corresponding schematics depicting lamellar stacks of PCL crystals and their structural parameters. The streak-like two-point reflections observed in Fig. 8a–c and d arise from oriented crystal stacks (as depicted in the bottom schematic of Fig. 8) [54]. In case of the less-oriented LiCoF, PEG200f_vlc, the SAXS pattern reveals two pairs of drop-shaped reflections (Fig. 8b). These patterns originate from stacks of parallel plates, where the transversal dimension of the crystals is significantly larger than the longitudinal dimension (aligned along the fiber axis) (as shown in the top schematic of Fig. 8) [54]. The pair of reflections that appears at higher angles cannot be attributed to higher order reflections, but rather suggests the presence of additional pairs of crystals. It is suspected that two distinct populations of crystal pairs exist

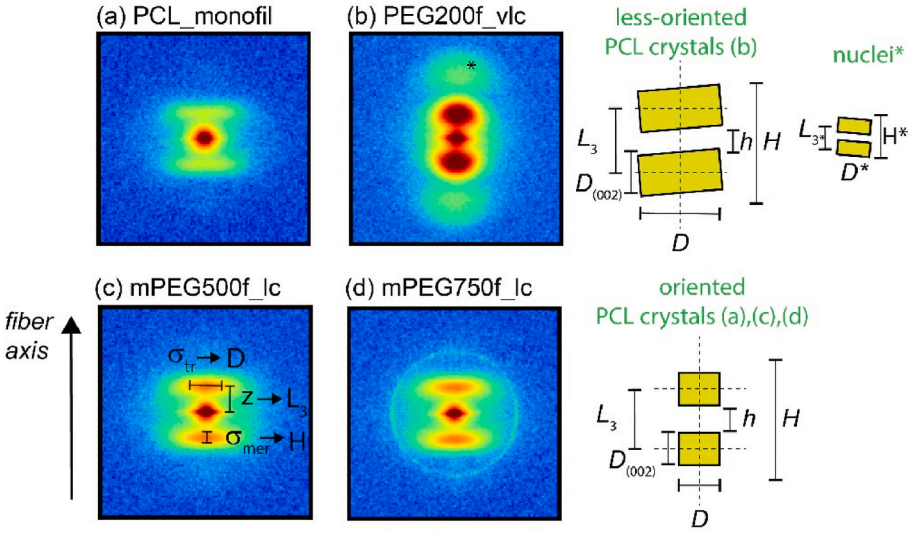

Fig. 8. Left panel: Measured SAXS patterns of (a) PCL monofilament and (b–d) various LiCoFs. Right panel: Schematics of a stack of PCL crystals (top: less-oriented crystals in (b) PEG200f_vlc, bottom: highly oriented crystals in (a, c, d)).

in this specific LiCoF: one population (referred to as nuclei*) with smaller crystals and another population (large crystals) with larger long spacings/coherence lengths. These crystals are not well-oriented in this particular filament due to the very low draw ratio (DR = 1.1).

In the LiCoF containing mPEG 750 (Fig. 8d), an additional distinct sharp ring was observed. This ring is most-likely a result of the mPEG 750 core and indicates an isotropic nanoscale crystal-like ordering, forming a superlattice with a periodicity of 5.9 nm. This ring is more prominent in the LiCoF with larger core than in the one with a smaller core (supporting information).

The complete set of measured SAXS patterns can be found in the supporting information. Structural parameters, including long-spacing L_3 (spacing between crystals along the fiber axis), transversal crystal width, D, and coherence length, H, have been determined from the SAXS patterns, following the methods described in previous publications [34, 35] (see supporting information for meridional and transversal projections). The crystal size along the fiber axis, $D(002)$, has been estimated from the full width at half-maximum of the (002) reflection in the WAXD pattern, applying Scherrer's equation [55] with the DIFFRAC. EVA (version 4.2., Bruker AXS, Karlsruhe, Germany) software to meridional profiles. The average spacing between crystals along the fiber axis, h, was determined by subtracting the crystal size $D(002)$ from the long spacing L_3. This crystal spacing parameter, h, plays a crucial role in understanding the drug-release diffusion mechanisms, as discussed in section 3.4. A summary of all structural parameters derived from SAXS and WAXD patterns can be found in Table 6, with further detailed information provided in the supporting information.

3.4. Diffusion trials

A variety of drug molecules were selected for the diffusion trials, each chosen for specific reasons: (i) fluorescein sodium salt was used in melt-spinning trials due to its ability to withstand high temperatures, (ii) ibuprofen has a small molecule size and is abundantly used as pain medication, (iii) methylene blue is a comparatively large molecule that visibly turns solutions to blue in high concentrations, and (iv) BSA-FITC is similar to human serum albumin (HSA), which is the most abundant protein in human plasma. In this study, the goal was to compare the diffusion properties of different molecules while using the same fibers; therefore liquid exchange was employed. Only fluorescein was directly released from the melt-spun LiCoFs, while all other drugs needed to be incorporated into the filaments through a liquid exchange, using different carrier liquids (mPEG500 for ibuprofen, Aqua stabil for methylene-blue, salt solution for BSA-FITC). Note that incorporating ibuprofen and other drug solutions directly into the core through the continuous melt-spinning process is planned for future trials.

Fig. 9 displays the measured absolute concentrations of fluorescein sodium salt that diffused from the melt-spun LiCoFs. The left side of the figure illustrates the diffused concentrations for the loops, while the right side shows those for the cut fiber pieces. The blue bars show the diffusion results for samples immersed for 24 h at room temperature, and the red bars show those for samples immersed for 24 h at 37 °C.

Table 6
Summary of structural parameters from oriented crystals, extracted from SAXS patterns (long-spacing, lateral crystal width and coherence length), and of crystal size/crystal spacing along meridian, extracted from WAXD patterns.

Label	L_3 (nm)	D (nm)	H (nm)	$D_{(002)}$ (nm)	h (nm)
PCL_monofil	14.5	6.8	25.4	10.5	4.0
PEG200f_vlc	15.6	21.3	31.6	10.8	4.8
	5.8[a]	6.6[a]	11.3[a]	NA[a]	NA[a]
sc and lc liquid-core fibers with DR = 5.0	14.4–14.7	9.4–10.7	28.4–31.0	7.2–9.7	4.8–7.5

[a] Second long spacing and coherence length.

Based on the data presented in Fig. 9, it can be inferred that a higher quantity of molecules diffused from the core at elevated temperatures (37 °C). This is explained by the higher mobility of molecules at elevated temperatures and by alterations in the PCL structure, which possesses a relatively low melting point at 60 °C. Furthermore, more molecules diffused out from fibers with larger cores (lc/vlc) as opposed to fibers with smaller core diameters (sc).

Fig. 10 presents the diffusion results for two types of LiCoFs (PEG200f_sc/vlc), filled with the original fluorescein sodium salt solution and with exchanged drug solutions containing ibuprofen, methylene blue or BSA-FITC. Measured absolute concentration values (μmol/l) are given in the supporting information. The results in Fig. 10 are expressed as percentages, p, of the diffused concentrations, calculated using Equation (2). Percentages of initial concentrations are provided to facilitate comparisons between the results from diffusion trials involving different drug molecules, as the initial concentrations varied among the drug solutions. Here, $V_{core} = \pi r^2 L$, represents the fiber core volume of length L (typically 20 cm) of immersed fibers in the Eppendorf tube. N_{init} is the initial number of moles of drug molecules within this fiber core volume, calculated from the prepared spinning concentration of the liquid in the LiCoFs (e.g., 0.1 wt% ibuprofen). N_{diff} is the number of moles of diffused molecules into the surrounding PBS medium of volume, V_{vial}, (typically 0.5 ml). Furthermore, Equation (3) is used to estimate the effective percentage, p^*, of the initial amount of moles of drug molecules that has diffused into the surrounding PBS medium. Note that this estimation can only be applied to cut fiber pieces, since the exact length immersed in the PBS is not known for loops. The diffusion is expected to continue until the equilibrium concentration is reached (Equation (4)), characterized by the concentration in the PBS medium being equal to that in the filament reservoir, driven by osmosis.

$$p\frac{N_{init}}{V_{core}} = \frac{N_{diff}}{V_{vial}} x100 \quad \text{(Eq. 2)}$$

$$p^* = \frac{N_{diff}}{N_{init}} x100 = p\frac{V_{vial}}{V_{core}} \quad \text{(Eq. 3)}$$

$$conc.^{eq} = \frac{N_{diff}^{eq}}{V_{vial}} = \frac{N_{init} - N_{diff}^{eq}}{V_{core}} \quad \text{(Eq. 4)}$$

Estimates of the effective percentage, p^*, of diffused drug molecules for cut fiber pieces indicate that about 70%–100% of ibuprofen and 60–90% of fluorescein molecules diffuse out within 24 h, whereas for methylene blue and BSA-FITC the values are lower (<50%). The faster diffusion of ibuprofen into PBS compared to fluorescein can be attributed to its smaller size and moderate hydrophobic nature, while fluorescein sodium salt is hydrophilic. PCL, being hydrophobic, tends to repel fluorescein sodium salt molecules. However, overall, the hydrophobic/hydrophilic nature of the drug seems not to exert a significant influence on the diffusion rate. Additionally, the fact that ibuprofen is less soluble in PBS than fluorescein sodium salt does barely affect the results at these low concentration levels.

The measured diffusion results of cut fiber samples were very reproducible with standard deviations lying below 0.02% (for, e.g., PEG200f_sc/lc). For the loops, however, standard deviations were larger (range: 0.01–0.13%), since the total length of immersed LiCoFs in the Eppendorf tubes varied from sample to sample and the amount of drug-reservoir (length of fiber ends outside of the PBS solution) also varied. However, the total length of the loops immersed in the PBS was always at least 20 cm. Considering this fact and the presence of a drug-reservoir in the fiber ends outside of the PBS solution, one would expect higher or similar diffusion values for loops, as compared to cut fiber pieces, in the cases where the drug molecules easily diffuse through the sheath. Indeed, this effect was observed for both, fluorescein sodium salt and ibuprofen, which easily diffuse through the sheath into the surrounding PBS. Interestingly, as shown in Fig. 10, methylene blue and BSA-FITC exhibit minimal diffusion through the PCL sheath in highly drawn

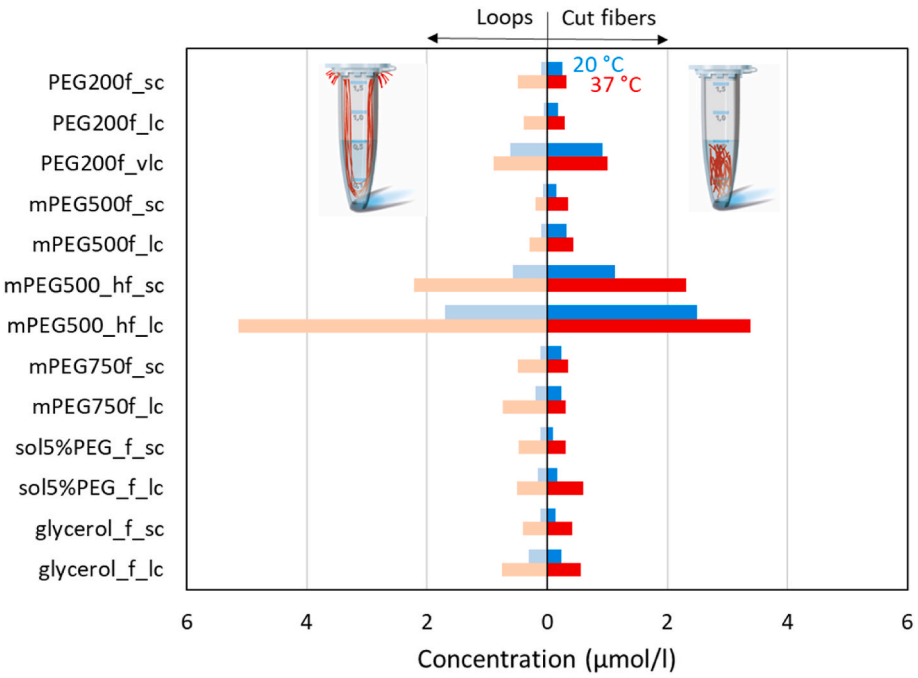

Fig. 9. Diffusion of fluorescein sodium salt out of melt-spun LiCoFs over 24 h at room temperature (blue bars) and 37 °C (red bars), respectively. Shown is the measured drug concentration in the receiving PBS. (For interpretation of the references to colour in this figure legend, the reader is referred to the Web version of this article.)

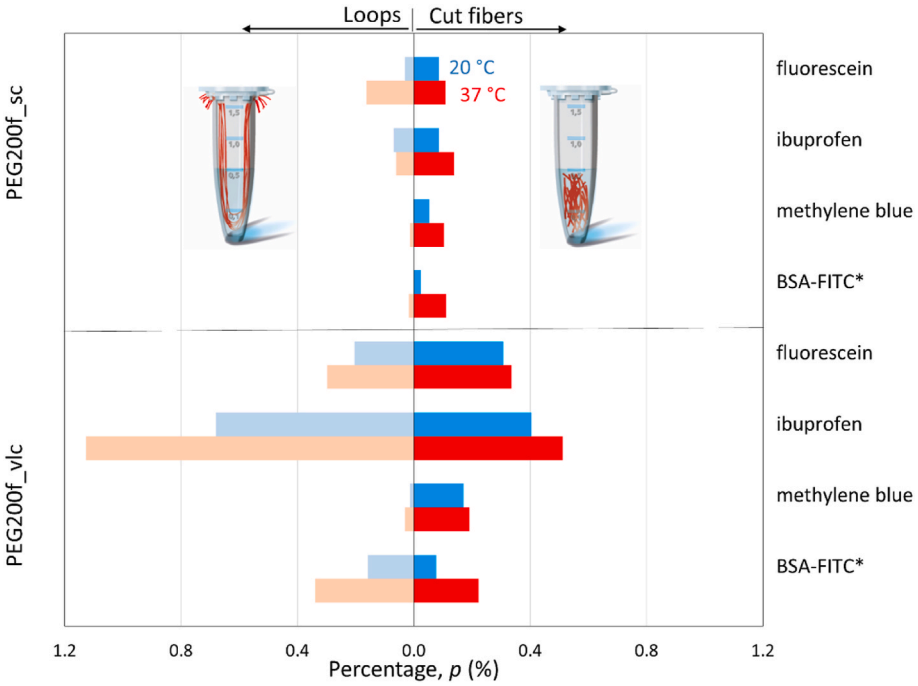

Fig. 10. Diffusion results of original melt-spun LiCoFs PEG200f_sc/vlc containing fluorescein sodium salt, and of the same LiCoFs with exchanged core liquids: 0.1 wt % ibuprofen in mPEG 500, 0.004 wt% methylene blue in water (aqua stabil) and 1 wt% BSA-FITC in NaCl solution. The percentage refers to *p*, calculated from Equation (2). *PEG200_vlc and PEG200_sc fibers were used for liquid exchange of BSA-FITC solution. (For interpretation of the references to colour in this figure legend, the reader is referred to the Web version of this article.)

filaments with small core (see also supporting information for similar results for larger core fibers, lc). Thus, in these highly drawn LiCoFs, small molecules with diameters below approximately 1 nm tend to diffuse out through the sheath into the surrounding PBS medium, while larger molecules preferentially migrate out through fiber ends, as depicted in Fig. 11. It's worth noting that drawn filaments have a relatively high crystallinity (~53–57%), with highly oriented crystals featuring spacings in the order of 4–7 nm. This structural configuration likely hinders the diffusion of larger molecules due to the limited spacing between crystals and their high degree of orientation.

The dimensions of the studied drug molecules including literature references are summarized in Table 7.

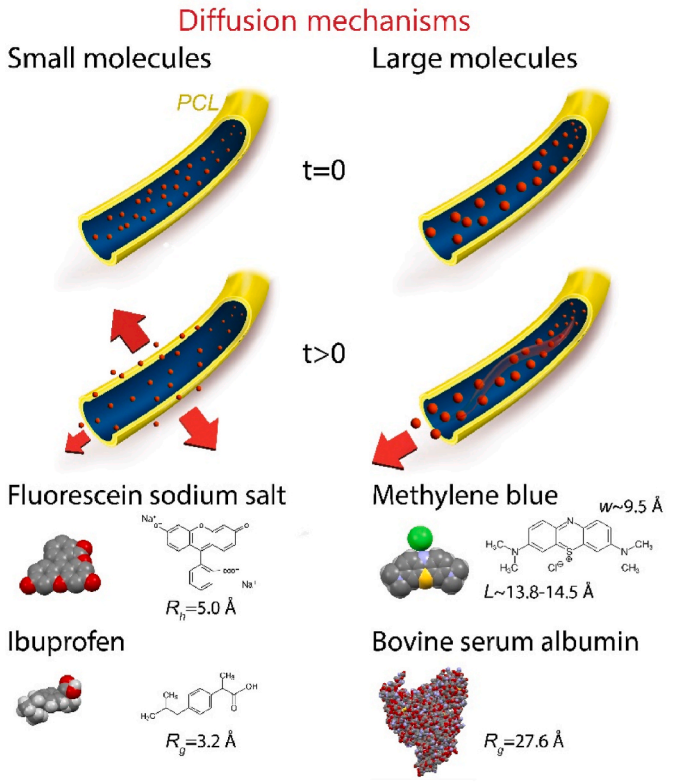

Fig. 11. Observed diffusion mechanisms for highly drawn LiCoFs. The diffusion results suggest that the mechanisms depend on the size of drug molecules. Left: Diffusion through PCL sheath of small molecules with dimensions smaller than approximately 1 nm. Right: Diffusion occurs mostly through fiber ends for larger molecules.

Table 7
Molecular dimensions of drug molecules including literature references.

Drug molecule	Molecule dimension	Literature reference
Fluorescein sodium salt	R_h = 5.0 Å	[56]
Ibuprofen	R_g = 3.2 Å	[57]
Methylene blue	Length ~ 13.82–14.47 Å Width ~ 9.5 Å	[58]
Bovine serum albumin (BSA), monomer	R_g = 27.6 Å Length ~140 Å, Width ~ 40 Å	[59–61]

Interestingly, in the marginally drawn filament (DR = 1.1) PEG200_vlc, BSA-FITC was able to diffuse through the PCL sheath, whereas methylene blue exhibited minimal diffusion. Methylene blue is a polar molecule, while PCL is a hydrophobic polymer, leading to PCL repelling methylene blue. On the other hand, BSA-FITC contains polar side chains, but it could still pass through the sheath of the less-oriented fiber, PEG200_vlc. Note that the precise dimensions of the purchased BSA-FITC protein are unknown and the FITC labeling may alter the dimensions of the monomeric BSA, which has a nominal molecular weight of 66 kDa. The monomeric BSA is hydrodynamically described as a prolate ellipsoid with major axis of 140 Å and minor axis of 40 Å [60,61]. However, being a protein, BSA might partially unfold and traverse the PCL sheath of the LiCoF with DR = 1.1. Additionally, for LiCoFs with DR = 1.1, the crystallinity is relatively high (~54%), but the crystals are comparatively large and less oriented, with larger spacings and a second population of small nuclei featuring small spacings. Consequently, more free space between crystal pairs can be expected, allowing BSA-FITC proteins to pass through. It is important to consider that the type of carrier liquid may influence the diffusion of drug molecules. Furthermore, although rather unlikely, small amounts of FITC may detach from BSA and diffuse out as well.

Diffusion rates of the drugs can be estimated applying Fick's first law of diffusion [62], which states the following:

$$J = -D\frac{d\varphi}{dx} \quad \text{(Eq. 5)}$$

The total diffusion through the polymer sheath can be approximated by:

$$J_{tot} = \frac{DA(c1 - c2)}{T} \quad \text{(Eq. 6)}$$

with J_{tot} representing the diffusion flux in (kg/s) and D the diffusion coefficient (m^2/s), A being the inner surface area (m^2) of the fiber (around the core), c_1, c_2 the concentrations (kg/m^3) on the inside and outside of the fiber and T the thickness of the sheath (m). The inner surface can be calculated as $2\pi rL+2\pi r^2$ for the cut fiber samples. Diffusion coefficients for fluorescein and ibuprofen in cut fiber pieces are estimated to be in the order of 10^{-15} to 10^{-14} m^2/s (D ~ 3.7e-15 m^2/s for e.g. PEG200f_sc at 20 °C: A ~7.8e-5 m^2 with (L ~ 20 cm, r ~ 31 μm), c_1 ~ 0.1124 kg/m^3 for 0.01 wt% fluorescein in PEG200, J ~5.6e-16 kg/s). Note that diffusion coefficients for the loops cannot be reliably estimated, since the length of the immersed loops was not well defined and the not-immersed fiber ends contain a reservoir of molecules. Future time-dependent drug-release studies as well as simulations will provide more insights into the diffusion processes at the molecular level.

4. Conclusion

We have successfully demonstrated the feasibility of melt-spinning drug-loaded LiCoFs, utilizing PCL as the sheath material. Fluorescein sodium salt was employed as a model drug, which was dissolved in various liquids. Several filaments with different liquid core materials and inner/outer diameters have been produced. The rheological properties of liquids and polymers have been investigated. Mechanical, thermal and structural properties of the melt-spun LiCoFs have been thoroughly examined through a series of tests, including tensile tests, differential scanning calorimetry, scanning electron microscopy and X-ray analytics.

Diffusion trials, involving fluorescence spectroscopy, have been performed in order to determine the diffusion of the fluorescein out of the filaments at room temperature and at elevated temperature (37 °C). Additionally, we conducted extensive diffusion trials involving the prior exchange of liquid cores with solutions containing ibuprofen, methylene blue, and BSA-FITC, followed by diffusion trials utilizing UPLC, UV–vis, and fluorescence spectroscopy.

The diffusion mechanism within LiCoFs is rather complex and is influenced by many factors such as structure of the sheath polymer (crystallinity, crystal spacing/orientation), surface/interfacial tension, temperature of surrounding media, type of carrier liquid (pH, viscosity), fiber core size/sheath thickness, drug molecule size/shape/flexibility/polarity and its interaction with the polymer sheath. Future modeling efforts aimed at elucidating time-dependent drug release through the PCL sheath will provide deeper insights into the interplay of these factors.

Findings reveal that for highly drawn LiCoFs, smaller molecules such as fluorescein sodium salt and ibuprofen predominantly diffuse out of the sheath. Conversely, larger molecules like methylene blue and BSA-FITC primarily diffuse through fiber ends. Additionally, we have demonstrated the feasibility of exchanging the liquid core in LiCoFs with other drug solutions using a pumping device.

Future melt-spinning trials will involve LiCoFs loaded with various drugs such as ibuprofen and corticosteroids, and will explore other polymers beyond PCL, such as poly(lactic acid) (PLA), Poly(glycolic

acid) (PGA), Poly(4-hydroxybutyrate) (P4HB) and Polypropylene (PP). Such studies will shed light on the limitations, including thermal degradation and drug solubility, associated with directly incorporating drugs into the liquid core during spinning. Furthermore, we intend to explore pressure-driven core liquid exchanges, involving living materials, enzymes, nanoparticles and more.

We firmly believe that these innovative melt-spun LiCoFs represent a significant advancement in the realm of medical textiles. Various medical products could potentially benefit from the drug reservoir, as well as from the durability, high tensile strength, and processability of these LiCoFs into textiles. Examples include surgical suture materials, single filament pumping devices, grafts, implantable or transdermal textiles for local drug delivery purposes, as well as anti-inflammatory, anti-bacterial, anti-viral, anti-coagulant and eventually anti-ageing textiles.

Funding sources

No funds, grants, or other support was received.

CRediT authorship contribution statement

Moritz Röthlisberger: Writing – review & editing, Validation, Software, Investigation, Formal analysis, Data curation, Conceptualization. **Sithiprumnea Dul:** Writing – review & editing, Investigation, Data curation. **Philipp Meier:** Writing – review & editing, Investigation, Data curation. **Giorgia Giovannini:** Writing – review & editing, Investigation, Data curation. **Rudolf Hufenus:** Writing – review & editing, Resources. **Edith Perret:** Writing – original draft, Visualization, Validation, Supervision, Software, Project administration, Investigation, Formal analysis, Data curation, Conceptualization.

Declaration of competing interest

The authors declare that they have no known competing financial interests or personal relationships that could have appeared to influence the work reported in this paper.

Data availability

Data will be made available on request.

Acknowledgments

We thank Benno Wüst for operating the melt-spinning plant, Markus Hilber for helping with tensile tests, Bianca Panchetti for performing tensile tests and preliminary diffusion trials, Patrick Rupper for helping with SEM measurements, and people from the center of X-ray analytics of Empa (Antonia Neels, Bruno Silva, Jonathan Avaro, Leonard Krupnik) for valuable discussions.

Appendix A. Supplementary data

Supplementary data to this article can be found online at https://doi.org/10.1016/j.polymer.2024.126885.

References

[1] M. Aquib, A.Z. Juthi, M.A. Farooq, M.G. Ali, A.H.W. Janabi, S. Bavi, P. Banerjee, R. Bhosale, R. Bavi, B. Wang, Advances in local and systemic drug delivery systems for post-surgical cancer treatment, J. Mater. Chem. B 8 (2020) 8507–8518, https://doi.org/10.1039/D0TB00987C.

[2] M. Rostamitabar, A.M. Abdelgawad, S. Jockenhoevel, S. Ghazanfari, Drug-eluting medical textiles: from fiber production and textile fabrication to drug loading and delivery, Macromol. Biosci. 21 (2021) 2100021, https://doi.org/10.1002/mabi.202100021.

[3] D. Massella, M. Argenziano, A. Ferri, J. Guan, S. Giraud, R. Cavalli, A.A. Barresi, F. Salaün, Bio-functional textiles: combining pharmaceutical nanocarriers with fibrous materials for innovative dermatological therapies, Pharmaceutics 11 (2019) 403, https://doi.org/10.3390/pharmaceutics11080403.

[4] D. Atanasova, D. Staneva, I. Grabchev, Textile materials modified with stimuli-responsive drug carrier for skin topical and transdermal delivery, Materials 14 (2021) 930, https://doi.org/10.3390/ma14040930.

[5] X.-Z. Sun, N. Wang, A thermosensitive textile-based drug delivery system for treating UVB-induced damage, Cellulose 27 (2020) 8329–8339, https://doi.org/10.1007/s10570-020-03334-z.

[6] A. Rohani Shirvan, A. Nouri, Chapter 13 - medical textiles, in: S. ul-Islam, B. S. Butola (Eds.), Advances in Functional and Protective Textiles, Woodhead Publishing, 2020, pp. 291–333.

[7] F. López-Saucedo, A. Ramos-Ballesteros, E. Bucio, Chapter 2 - functionalization of sutures, in: S. Thomas, P. Coates, B. Whiteside, B. Joseph, K. Nair (Eds.), Advanced Technologies and Polymer Materials for Surgical Sutures, Woodhead Publishing, 2023, pp. 19–44.

[8] R. Shah, L. Taylor, M. Saeinasab, X. Zhang, W. Zhang, K. Nair, F. Sefat, Chapter 7 - bioactive sutures: advances in surgical suture functionalization, in: S. Thomas, P. Coates, B. Whiteside, B. Joseph, K. Nair (Eds.), Advanced Technologies and Polymer Materials for Surgical Sutures, Woodhead Publishing, 2023, pp. 149–169.

[9] M. Amjadi, S. Sheykhansari, B.J. Nelson, M. Sitti, Recent advances in wearable transdermal delivery systems, Adv. Mater. 30 (2018) 1704530, https://doi.org/10.1002/adma.201704530.

[10] S. Chatterjee, P. Chi-leung Hui, Review of stimuli-responsive polymers in drug delivery and textile application, Molecules 24 (2019) 2547, https://doi.org/10.3390/molecules24142547.

[11] R. Hufenus, L. Gottardo, A.A. Leal, A. Zemp, K. Heutschi, P. Schuetz, V.R. Meyer, M. Heuberger, Melt-spun polymer fibers with liquid core exhibit enhanced mechanical damping, Mater. Des. 110 (2016) 685–692, https://doi.org/10.1016/j.matdes.2016.08.042.

[12] A.A. Leal, M. Naeimirad, L. Gottardo, P. Schuetz, A. Zadhoush, R. Hufenus, Microfluidic behavior in melt-spun hollow and liquid core fibers, Int. J. Polym. Mater. 65 (2016) 451–456, https://doi.org/10.1080/00914037.2015.1129957.

[13] R. Hufenus, M. Heuberger, A.A. Leal, Multifunctional liquid-core melt-spun filaments, Chem. Fibers Int. 68 (2018) 181–182.

[14] R. Hufenus, J. Hofmann, A. Gooneie, Fine liquid-core polymer fibers for microhydraulic applications: a versatile process design, Mater. Des. 222 (2022) 111077, https://doi.org/10.1016/j.matdes.2022.111077.

[15] K. Jakubowski, W. Kerkemeyer, E. Perret, M. Heuberger, R. Hufenus, Liquid-core polymer optical fibers for luminescent waveguide applications, Mater. Des. 196 (2020) 109131, https://doi.org/10.1016/j.matdes.2020.109131.

[16] B. Pant, M. Park, S.J. Park, Drug delivery applications of core-sheath nanofibers prepared by coaxial electrospinning: a review, Pharmaceutics 11 (2019) 305, https://doi.org/10.3390/pharmaceutics11070305.

[17] Y. Dai, J. Ahmed, M. Edirisinghe, Pressurized gyration: fundamentals, advancements, and future, Macromol. Mater. Eng. 308 (2023) 2300033, https://doi.org/10.1002/mame.202300033.

[18] T.J. Sill, H.A. von Recum, Electrospinning: applications in drug delivery and tissue engineering, Biomaterials 29 (2008) 1989–2006, https://doi.org/10.1016/j.biomaterials.2008.01.011.

[19] S. Saghazadeh, C. Rinoldi, M. Schot, S.S. Kashaf, F. Sharifi, E. Jalilian, K. Nuutila, G. Giatsidis, P. Mostafalu, H. Derakhshandeh, K. Yue, W. Swieszkowski, A. Memic, A. Tamayol, A. Khademhosseini, Drug delivery systems and materials for wound healing applications, Adv. Drug Deliv. Rev. 127 (2018) 138–166, https://doi.org/10.1016/j.addr.2018.04.008.

[20] Z. Moazzami Goudarzi, M. Soleimani, L. Ghasemi-Mobarakeh, P. Sajkiewicz, F. Sharifianjazi, A. Esmaeilkhanian, S. Khaksar, Control of drug release from cotton fabric by nanofibrous mat, Int. J. Biol. Macromol. 217 (2022) 270–281, https://doi.org/10.1016/j.ijbiomac.2022.06.138.

[21] R. Hufenus, Y. Yan, M. Dauner, T. Kikutani, Melt-spun fibers for textile applications, Materials 13 (2020) 4298, https://doi.org/10.3390/ma13194298.

[22] B.S. Gupta, 1 - manufacture, types and properties of biotextiles for medical applications, in: M.W. King, B.S. Gupta, R. Guidoin (Eds.), Biotextiles as Medical Implants, Woodhead Publishing, Philadelphia, USA, 2013, pp. 3–47.

[23] C.C. Chu, 11 - materials for absorbable and nonabsorbable surgical sutures, in: M. W. King, B.S. Gupta, R. Guidoin (Eds.), Biotextiles as Medical Implants, Woodhead Publishing, Philadelphia, USA, 2013, pp. 275–334.

[24] B.S. Gupta, 14 - small-diameter arterial grafts using biotextiles, in: M.W. King, B. S. Gupta, R. Guidoin (Eds.), Biotextiles as Medical Implants, Woodhead Publishing, Philadelphia, USA, 2013, pp. 408–433.

[25] C.R. Carvalho, J.M. Oliveira, R.L. Reis, Modern trends for peripheral nerve repair and regeneration: beyond the hollow nerve guidance conduit, Front. Bioeng. Biotechnol. 7 (2019) 337, https://doi.org/10.3389/fbioe.2019.00337.

[26] V. Chiono, G. Vozzi, F. Vozzi, C. Salvadori, F. Dini, F. Carlucci, M. Arispici, S. Burchielli, F. Di Scipio, S. Geuna, M. Fornaro, P. Tos, S. Nicolino, C. Audisio, I. Perroteau, A. Chiaravalloti, C. Domenici, P. Giusti, G. Ciardelli, Melt-extruded guides for peripheral nerve regeneration. Part I: poly(ε-caprolactone), Biomed. Microdevices 11 (2009) 1037, https://doi.org/10.1007/s10544-009-9321-9.

[27] T. Tat, G. Chen, X. Zhao, Y. Zhou, J. Xu, J. Chen, Smart textiles for healthcare and sustainability, ACS Nano 16 (2022) 13301–13313, https://doi.org/10.1021/acsnano.2c06287.

[28] L.M. Zhu, D.G. Yu, 9 - drug delivery systems using biotextiles, in: M.W. King, B. S. Gupta, R. Guidoin (Eds.), Biotextiles as Medical Implants, Woodhead Publishing, 2013, pp. 213–231.

[29] Y. Zhang, W. Fan, Y. Sun, W. Chen, Y. Zhang, Application of antiviral materials in textiles, Review 10 (2021) 1092–1115, https://doi.org/10.1515/ntrev-2021-0072.

[30] A. Sultana, M. Zare, V. Thomas, T.S.S. Kumar, S. Ramakrishna, Nano-based drug delivery systems: conventional drug delivery routes, recent developments and future prospects, Med. Drug Discov. 15 (2022) 100134, https://doi.org/10.1016/j.medidd.2022.100134.
[31] J. Pal, N. Kankariya, S. Sanwaria, B. Nandan, R.K. Srivastava, Control on molecular weight reduction of poly(ε-caprolactone) during melt spinning — a way to produce high strength biodegradable fibers, Mater. Sci. Eng. C 33 (2013) 4213–4220, https://doi.org/10.1016/j.msec.2013.06.011.
[32] M.M. Hall, V.G. Veeraraghavan, H. Rubin, P.G. Winchell, The approximation of symmetric X-ray peaks by Pearson type VII distributions, J. Appl. Crystallogr. 10 (1977) 66–68, https://doi.org/10.1107/s0021889877012849.
[33] J.J. Hermans, P.H. Hermans, D. Vermaas, A. Weidinger, Quantitative evaluation of orientation in cellulose fibres from the X-ray fibre diagram, Recl. Trav. Chim. Pays-Bas J. R. Neth. Chem. Soc. 65 (1946) 427–447, https://doi.org/10.1002/recl.19460650605.
[34] F. Selli, U.H. Erdoğan, R. Hufenus, E. Perret, Mesophase in melt-spun poly (ε-caprolactone) filaments: structure–mechanical property relationship, Polymer 206 (2020) 122870, https://doi.org/10.1016/j.polymer.2020.122870.
[35] F. Selli, U.H. Erdoğan, R. Hufenus, E. Perret, Properties, X-ray data and 2D WAXD fitting procedures of melt-spun poly(ε-caprolactone), Data Brief 32 (2020) 106223, https://doi.org/10.1016/j.dib.2020.106223.
[36] A. Avella, R. Mincheva, J.-M. Raquez, G. Lo Re, Substantial effect of water on radical melt crosslinking and rheological properties of poly(ε-caprolactone), Polymers 13 (2021) 491, https://doi.org/10.3390/polym13040491.
[37] S. Trinkle, C. Friedrich, Van Gurp-Palmen-plot: a way to characterize polydispersity of linear polymers, Rheol. Acta 40 (2001) 322–328, https://doi.org/10.1007/s003970000137.
[38] C.A. Schneider, W.S. Rasband, K.W. Eliceiri, NIH Image to ImageJ: 25 years of image analysis, Nat. Methods 9 (2012) 671–675, https://doi.org/10.1038/nmeth.2089.
[39] S.F. Williams, S. Rizk, D.P. Martin, Poly-4-hydroxybutyrate (P4HB): a new generation of resorbable medical devices for tissue repair and regeneration 58 (2013) 439–452, https://doi.org/10.1515/bmt-2013-0009.
[40] Y. Chatani, Y. Okita, H. Tadokoro, Y. Yamashita, Structural studies of polyesters. III. Crystal structure of poly-ε-caprolactone, Polym. J. 1 (1970) 555, https://doi.org/10.1295/polymj.1.555.
[41] C.F. Macrae, I. Sovago, S.J. Cottrell, P.T.A. Galek, P. McCabe, E. Pidcock, M. Platings, G.P. Shields, J.S. Stevens, M. Towler, P.A. Wood, Mercury 4.0: from visualization to analysis, design and prediction, J. Appl.Cryst 53 (2020) 226–235, https://doi.org/10.1107/S1600576719014092.
[42] K. Sharma, O. Braun, S. Tritsch, R. Muff, R. Hufenus, E. Perret, 2D Raman, ATR-FTIR, WAXD, SAXS and DSC data of PET mono- and PET/PA6 bicomponent filaments, Data Brief 38 (2021) 107416, https://doi.org/10.1016/j.dib.2021.107416.
[43] E. Perret, F.A. Reifler, R. Hufenus, O. Bunk, M. Heuberger, Modified crystallization in PET/PPS bicomponent fibers revealed by small-angle and wide-angle X-ray scattering, Macromolecules 46 (2013) 440–448, https://doi.org/10.1021/ma3021213.
[44] E. Perret, O. Braun, K. Sharma, S. Tritsch, R. Muff, R. Hufenus, High-resolution 2D Raman mapping of mono- and bicomponent filament cross-sections, Polymer 229 (2021) 124011, https://doi.org/10.1016/j.polymer.2021.124011.
[45] F. Selli, R. Hufenus, A. Gooneie, U.H. Erdoğan, E. Perret, Structure-Property relationship in melt-spun poly(hydroxybutyrate-co-3-hexanoate) monofilaments, Polymers 14 (2022) 200, https://doi.org/10.3390/polym14010200.
[46] E. Perret, F.A. Reifler, A. Gooneie, K. Chen, F. Selli, R. Hufenus, Structural response of melt-spun poly(3-hydroxybutyrate) fibers to stress and temperature, Polymer 197 (2020) 122503, https://doi.org/10.1016/j.polymer.2020.122503.
[47] E. Perret, F.A. Reifler, A. Gooneie, R. Hufenus, Tensile study of melt-spun poly(3-hydroxybutyrate) P3HB fibers: reversible transformation of a highly oriented phase, Polymer 180 (2019) 121668, https://doi.org/10.1016/j.polymer.2019.121668.
[48] E. Perret, K. Sharma, S. Tritsch, R. Hufenus, Reversible mesophase in stress-annealed poly(3-hydroxybutyrate) fibers: a synchrotron x-ray and polarized ATR-FTIR study, Polymer 231 (2021) 124141, https://doi.org/10.1016/j.polymer.2021.124141.
[49] E. Perret, R. Hufenus, Insights into strain-induced solid mesophases in melt-spun polymer fibers, Polymer 229 (2021) 124010, https://doi.org/10.1016/j.polymer.2021.124010.
[50] E. Perret, R. Hufenus, Fitting of 2D WAXD data: mesophases in polymer fibers, Data Brief 39 (2021) 107466, https://doi.org/10.1016/j.dib.2021.107466.
[51] E. Perret, F.A. Reifler, A. Gooneie, K. Chen, F. Selli, R. Hufenus, X-Ray Data about the Structural Response of Melt-Spun Poly(3-Hydroxybutyrate) Fibers to Stress and Temperature Data in Brief, vol. 31, 2020 105675, https://doi.org/10.1016/j.dib.2020.105675.
[52] E. Perret, F.A. Reifler, A. Gooneie, R. Hufenus, X-ray data from a cyclic tensile study of melt-spun poly(3-hydroxybutyrate) P3HB fibers: a reversible mesophase, Data Brief 25 (2019) 104376, https://doi.org/10.1016/j.dib.2019.104376.
[53] E. Perret, K. Sharma, S. Tritsch, R. Hufenus, WAXD, polarized ATR-FTIR and DSC data of stress-annealed poly(3-hydroxybutyrate) fibers, Data Brief 39 (2021) 107523, https://doi.org/10.1016/j.dib.2021.107523.
[54] V.I. Gerasimov, Y.V. Genin, D.Y. Tsvankin, Small-angle X-Ray study of deformed bulk polyethylene, J. Polym. Sci. B Polym. Phys. 12 (1974) 2035–2046, https://doi.org/10.1002/pol.1974.180121006.
[55] A. Guinier, X-Ray Diffraction, W. H. Freeman, San Francisco, CA, USA, 1963.
[56] M.B. Mustafa, D.L. Tipton, M.D. Barkley, P.S. Russo, F.D. Blum, Dye diffusion in isotropic and liquid-crystalline aqueous (hydroxypropyl)cellulose, Macromolecules 26 (1993) 370–378, https://doi.org/10.1021/ma00054a017.
[57] E.P. Raman, T. Takeda, D.K. Klimov, Molecular dynamics simulations of Ibuprofen binding to Abeta peptides, Biophys. J. 97 (2009) 2070–2079, https://doi.org/10.1016/j.bpj.2009.07.032.
[58] P. Jia, H. Tan, K. Liu, W. Gao, Removal of methylene blue from aqueous solution by bone char, Appl. Sci. 8 (2018) 1903, https://doi.org/10.3390/app8101903.
[59] D.M. Smilgies, E. Folta-Stogniew, Molecular weight-gyration radius relation of globular proteins: a comparison of light scattering, small-angle X-ray scattering and structure-based data, J. Appl. Crystallogr. 48 (2015) 1604–1606, https://doi.org/10.1107/s1600576715015551.
[60] P.G. Squire, P. Moser, C.T. O'Konski, Hydrodynamic properties of bovine serum albumin monomer and dimer, Biochemistry 7 (1968) 4261–4272, https://doi.org/10.1021/bi00852a018.
[61] A.K. Wright, M.R. Thompson, Hydrodynamic structure of bovine serum albumin determined by transient electric birefringence, Biophys. J. 15 (1975) 137–141, https://doi.org/10.1016/S0006-3495(75)85797-3.
[62] A. Fick, On liquid diffusion, J. Membr. Sci. 100 (1995) 33–38, https://doi.org/10.1016/0376-7388(94)00230-V.